water

MDPI

Article

# Quantitative Estimation of Soil Salinization in an Arid Region of the Keriya Oasis Based on Multidimensional Modeling

**Nijat Kasim [1,†], Balati Maihemuti [2,*,†], Rukeya Sawut [3], Abdugheni Abliz [2], Cui Dong [1] and Munira Abdumutallip [4]**

1 College of Biology and Geography, Yili Normal University, Yining 835000, China; NejatKasim@126.com (N.K.); cuidongw@126.com (C.D.)
2 College of Resources and Environmental Sciences, Xinjiang University, Urumqi 830046, China; Abduhini0997@126.com
3 Navigation College, Dalian Maritime University, Dalian 116026, China; Rukeyars@163.com
4 Shanghai Key Laboratory of Atmospheric Particle Pollution and Prevention (LAP3), Department of Environmental Science and Engineering, Institute of Atmospheric Sciences, Fudan University, Shanghai 200438, China; munira@fudan.edu.cn
* Correspondence: mahmut_barat@126.com
† These authors contributed equally to this work.

Received: 11 February 2020; Accepted: 11 March 2020; Published: 20 March 2020


**Abstract:** Soil salinity is one of the major factors causing land degradation and desertification on earth, especially its important damage to farming activities and land-use management in arid and semiarid regions. The salt-affected land is predominant in the Keriya River area of Northwestern China. Then, there is an urgent need for rapid, accurate, and economical monitoring in the salt-affected land. In this study, we used the electrical conductivity (EC) of 353 ground-truth measurements and predictive capability parameters of WorldView-2 (WV-2), such as satellite band reflectance and newly optimum spectral indices (OSI) based on two dimensional and three-dimensional data. The features of spectral bands were extracted and tested, and different new OSI and soil salinity indices using reflectance of wavebands were built, in which spectral data was pre-processed (based on First Derivative (R-FD), Second Derivative (R-SD), Square data (R-SQ), Reciprocal inverse (1/R), and Reciprocal First Derivative (1/R-FD)), utilizing the partial least-squares regression (PLSR) method to construct estimation models and mapping the regional soil-affected land. The results of this study are the following: (a) the new OSI had a higher relevance to EC than one-dimensional data, and (b) the cross-validation of established PLSR models indicated that the β-PLSR model based on the optimal three-band index with different process algorithm performed the best result with $R^2_V = 0.79$, Root Mean Square Errors ($RMSE_V$) = 1.51 dS·m$^{-1}$, and Relative Percent Deviation (RPD) = 2.01 and was used to map the soil salinity over the study site. The results of the study will be helpful for the study of salt-affected land monitoring and evaluation in similar environmental conditions.

**Keywords:** soil salinization; optimized spectral algorithm; Keriya River; EC; arid region

## 1. Introduction

Soil salinization is one of the most serious damaging environmental problems worldwide, especially in a hyperarid region [1]. Approximately 1.128 billion hectares of global lands were affected by soil salinization [2], and in China, salinized areas accounting for approximately 9 percent of the national land resources [3,4]. Major causes of soil salinization can be separated into two ways: one way from primitive soluble saline water, scarce precipitation, and intense evaporation

and the other way from shallow groundwater levels, excessive agricultural activities, and flooding irrigation agriculture [5,6]. Quantitative analysis of salt-affected land is one of the effective methods to evaluate the extent of soil salinization, and there is a wide divergence in the embedding temporal and spatial dimensions.

Soil salinization is also an important factor leading to land desertification and degradation. Excessive soil salinity poses a serious threat to the healthy growth of crops and vegetation and to the sustainable development of eco-environmental systems [7]. There is an urgent need for dynamic monitoring, which can provide a sufficient understanding of the importance of current soil salinization. It is very important in sustainable development for the regional agricultural and eco-environmental system. Its help to control soil salinization is also further effective in soil remediation and land rehabilitation [8].

There were numerous methods to detect soil salinization; among them, soil electrical conductivity (EC) field measurements has a strong relationship with soil salinization, which is often used for dynamic monitoring of salt-affected land [9]. However, the EC method detecting soil salinity is highly accurate, but the shortcomings of this method are the too slow processing, discontinuity, limited space, and financially expensive; furthermore, it is difficult to carry out regional scientific research. Nowadays, remote sensing (RS) technology provides a more efficient way to evaluate soil salinization; the advantages of this method include the quick processing, low cost, efficiency, and use of historical analyses compared to conventional methods. It also exposes the spatiotemporal variation of soil salinization from the past to the present [4].

The optimal spectral indices that combined with various spectral reflectances could express more unexpressed spectral features and could further improve the correlation between remote sensing data and the ground targets [10]. The wavelengths (red (R), blue (B), near-infrared (NIR), and green (G)) of satellite images have different spectral behaviors on varying degrees of salinization so that the salinity map of the soil is detected based on optimum spectral indices.

Research of soil salinity monitoring and mapping based on various spectral soil salinity indices has attracted many scientists. Khan's research team assessed the hydro-saline land degradation by using a simple approach of remote sensing indicators [11,12]. Allbed and their colleagues evaluated the soil salinity using vegetation indices derived from IKONOS high spatial resolution imageries [13]. Triki's research team used Landsat 8 data to generate nineteen spectral indices (Normalized Difference Vegetation Index (NDVI), Soil index (SI1, SI2, SI3, SI), soil adjusted vegetation index (SAVI), SI1-IDNP, ASTER-SI, SI-VIR, Intensity Index (Int1, Int2), and Band Index (BI).), analyzed the correlations between reflectance indices and EC measured on laboratory, and demonstrated that the Short Wave Infrared (SWIR) offers a good correlation with −57% [14,15]. The research based on spectral indices has shown a variable degree of success, and spectral indices have been successfully used as indirect indicators for monitoring and mapping soil salinity [13,15].

Agriculture in the Keriya Oasis is the primary style of land use, which mainly relies on the water resources from the Keriya River for irrigation. A combination of the hyper dry arid climate, geomorphological, soil formation conditions, and shallow groundwater levels facilitated the movement of dissolved salts to the land surface. Our research team also did some study on soil salinity detection and maps on the Keriya River site [16,17]. We found that such phenomena caused soil salinization and desertification, especially in the transitional belt between the oasis and the desert. The riparian ecosystem of Keriya River is very fragile due to the hyper dry climate, low precipitation, strongly potential evaporation, and active wind erosion. Most of the soils in these regions are sandy, silty sand, coarse in texture, and low in nutrients [16]. Therefore, it is necessary to offer data sources and parameters (based on the Multi-Spectral Instrument (MSI) onboard WV-2 image) for the detecting and mapping of soil salinity for Keriya Oasis and for avoiding and preventing disasters and risks from soil salinization.

In this study, we utilized the high spatial resolution of WorldView-2 satellite images to improve the estimation performance. The main aim of this study is to develop new combination spectral

indices and to further enhance the correlation coefficient with specific data; this study would ultimately contribute to detecting and mapping soil salinity in the Keriya River site. An intensive understanding of the salt dynamics in the soil profile and the timely monitoring of the spatial distribution of soil salinity has become an imperative task for both agricultural sustainability and ecological stability.

## 2. Materials and Methods

### *2.1. Study Area*

The Keriya River is located in the southern part of the Taklamakan Desert in the Xinjiang Uyghur Autonomous Region of China [17,18]. This river originates from the Kunlun Mountains and flows through the Keriya Oasis, and after approximately 700 km, the river ends in the hinterland of the Taklamakan Desert [18]. This region has a temperate continental arid climate that is characterized by hyper aridity. On average, the region receives 45 mm of precipitation annually but experiences mean evaporation of 2600 mm annually, which is more than 50 times the mean annual precipitation [16]. This oasis is located on a fluvial plain with relatively flat terrain, loose soil, high salt concentrations, and low soil fertility [18]. Sparsely vegetated riparian areas are covered with dominant desert species such as *Phragmites australis*, *Tamarix chinensis*, *Populus euphratica*, *Alhagi sparsifolia*, *Karelina capsica*, and *Kalidium gracile* [19]. The sample plot was selected in the lower riparian area of the Keriya River because of the high spatial variability in soil salinity, relatively flat terrain, and sparse vegetation cover observed during the pilot investigation (see Figure 1). Additionally, the riparian ecosystem became more vulnerable due to the intensified agricultural activities and deep drainage systems in the upper reaches which brought more leached saline water to the lower reaches.

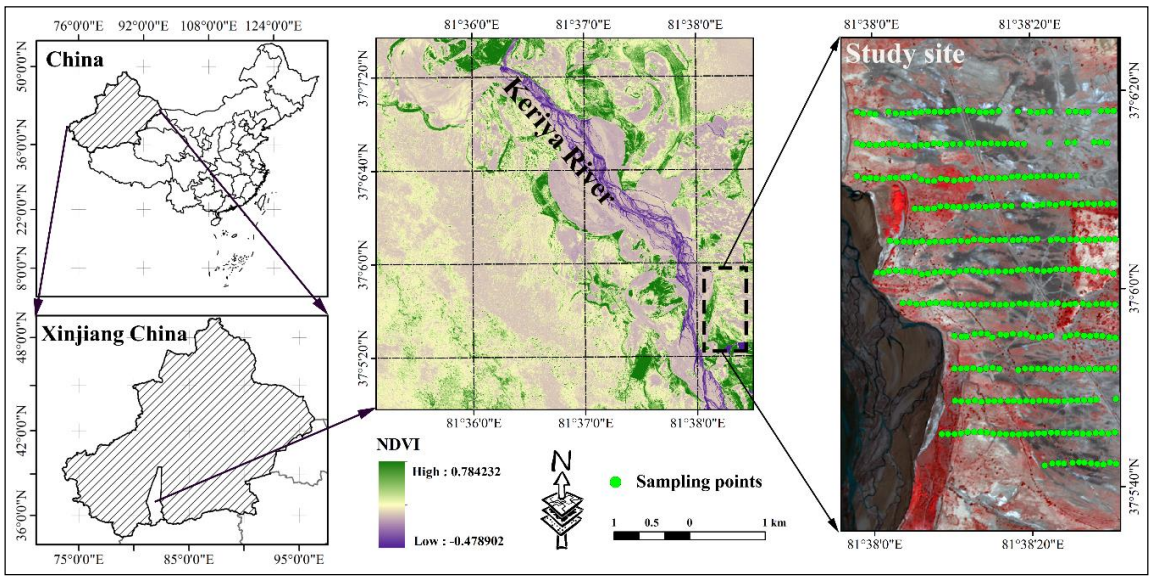


**Figure 1.** Location of study area and distribution of sampling points.

### *2.2. Field Measurement*

The sample plot was surveyed using an EM38-MK2 m (Geonics Ltd., Mississauga, ON, Canada) connected with global positioning system (GPS) and data logging unit. Transects were chosen based on their geographic locations, local soil conditions, degree of vegetation, and site accessibility. During the surveying, field measurements were made strictly following the protocols and guidelines for Electromagnetic Interference (EMI) field-scale measurements outlined by Corwin [20]. The vertical dipole orientation mode of the EM38-MK2 m, with one transmitter coil and two receiver coils that are separated from the transmitter coil at distances of 0.5 m and 1.0 m (investigation depth of 0.75 m and 1.5 m), were used, and measurements were taken at 353 points along 12 transects (see in Figure 1).

Raw binary data files (N38) were converted to American Standard Code for Information Interchange (ASCII) files (M38) in the DAT38MK2 software®. An average from five readings at each sample point was calculated as the representative value of the apparent electrical conductivity.

### 2.3. Selection of Spectral Indices and Sensitive Bands

The satellite data (WorldView-2 (WV-2) multispectral data) acquisition and processing in this study were as follows:

(1) WV-2 multispectral data includes multispectral bands and was described in Table 1. The images were geo-rectified to a Universal Transverse Mercator (UTM) coordinate system using the World Geodetic System (WGS) 1984 datum assigned to north UTM zone 44 [17].
(2) Spectral radiometric calibration and atmospheric and Geometric corrections were performed on the WV-2 [21].
(3) The FLAASH model was used to eliminate atmospheric and adjacency effects for images using the Environmental for Visualizing Images (ENVI 5.3, EXELIS VIS) software package® [22]. The WV-2 image was resampled into 2-m resolution, and the River channel with water bodies was clipped out due to the inaccessibility for sampling.

**Table 1.** WorldView-2 spectral details.

| Bands | Wavelength (nm) | Resolution |
|---|---|---|
| Coastal | 400–450 | Multispectral: 1.85 m GSD at nadir, 2.07 m GSD at 20° off-nadir. |
| Blue | 450–510 | |
| Green | 510–580 | |
| Yellow | 585–625 | |
| Red | 630–690 | |
| Red Edge | 705–745 | Panchromatic: 0.46 m GSD at nadir, 0.52 m GSD at 20° off-nadir. |
| Near-IR1 | 770–895 | |
| Near-IR2 | 860–1040 | |

One of the most effective approaches for exploring significant relationships between the electrical conductivity data and hyperspectral data is conducting a comparative analysis of Ratio index (RI), Simple normalized index (NDI), and Soil salinization index ($SI_1$ and $SI_2$), which are calculated from narrowband reflectance factor spectra. We identified the wavelengths or spectral indices (showed in Table 2). The optimized spectral indices (OSI) were applied to identify optimal wavelengths or indices. The spectral indices are defined as follows:

**Table 2.** Optimized spectral indices selected in this study.

| Optimized Spectral Index | Abbreviation | Equation | Reference |
|---|---|---|---|
| Ratio index | RI | $R_{\lambda 1}/R_{\lambda 2}$ | [23] |
| Normalized difference index | NDI | $(R_{\lambda 1} - R_{\lambda 2})/(R_{\lambda 1} - R_{\lambda 2})$ | |
| Soil salinization index1 | $SI_1$ | $Sqrt\ (R_{\lambda 1}{}^2 \times R_{\lambda 2}{}^2)$ | |
| Soil salinization index2 | $SI_2$ | $Sqrt\ (R_{\lambda 1}{}^2 + R_{\lambda 2}{}^2 + R_{\lambda 3}{}^2)$ | [11] |

Note: $R$ is the spectral reflectance value, and the subscripts $\lambda_1$, $\lambda_2$, and $\lambda_3$ are wavelengths in nanometers (nm).

### 2.4. Model Generation and Data Analysis

To investigate soil salinity using WorldView-2 data and soil salinity (EC) data in the study site, the workflow was presented in Figure 2 and described in the following sections.

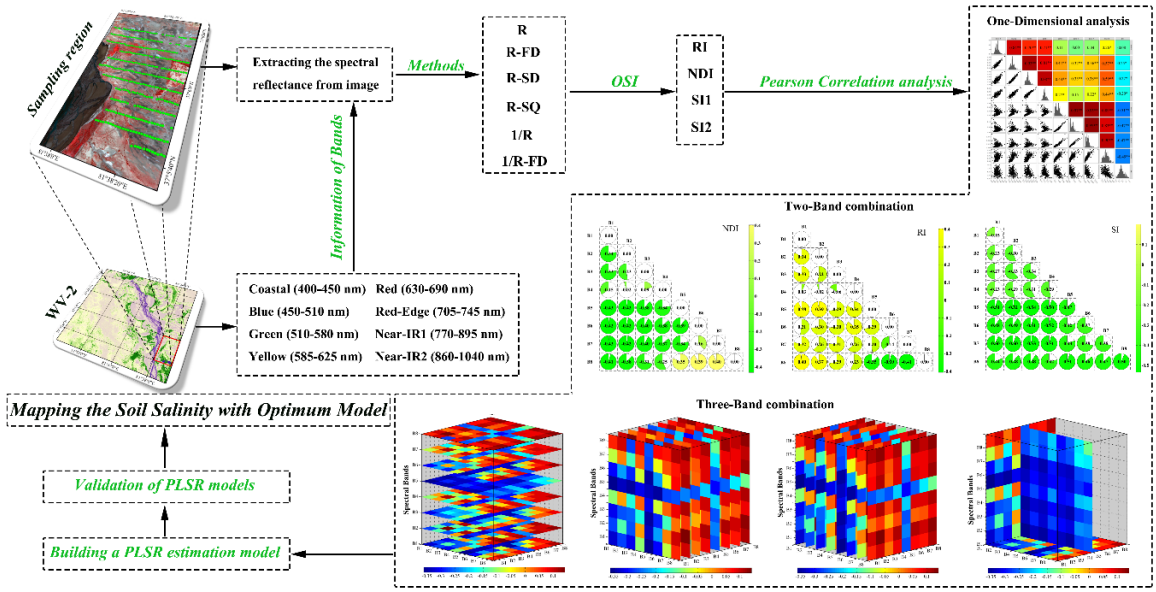


**Figure 2.** Overall workflow of the study.

### *2.5. Partial Least-Squares Regression*

Partial least-squares regression (PLSR) is a multivariate regression method that specifies a linear relationship between a set of dependent response variables, $Y$, and a set of predictor variables, $X$ [24,25]. To select the optimal number of factors and to avoid overfitting, we calibrated the model by an iterative leave-one-out cross-validation criterion called the "minimum predicted residual sum of squares". Root mean square error (RMSE) was minimized by iteratively leaving one sample out of the calibration dataset and by calibrating the model from the remaining dataset [17,25–27].

### *2.6. Model Evaluation*

Validation of the models is an important step to ensure models quality [28–30] once all the developed models were verified by authentication methods (showed in Table 3) as follows:

(1) A high coefficient of determination ($R^2$), indicating a strong linear relationship.

(2) Low Root Mean Square Errors (RMSE) of the model's variables, indicating that the low error between measured and predicted data were calculated by the equation listed in Table 3.

(3) Relative Percent Deviation (RPD), indicating the predictive ability of the model. Its computation process is the ratio between standard deviation (SD) and standard error of prediction (SEP). According to the predictive ability of the model, the RPD is divided into three categories: (1) The value of RPD exceeds 2.0, indicating a model with better predictive ability. (2) The RPD values ranging from 1.4 to 2.0 represent a model with general predictive ability. (3) The RPD value is less than 1.4, indicating that it has poor predictive ability.

**Table 3.** Model evaluation index.

| Index | Equation |
|---|---|
| Coefficient of Determination | $R^2 = \left[\frac{\sum_{i=1}^{N}(x_i-\bar{x})(y_i-\bar{y})}{\sqrt{\sum_{i=1}^{N}(x_i-\bar{x})^2+\sum_{i=1}^{N}(y_i-\bar{y})^2}}\right]^2$ |
| Root Mean Square Error | $\mathrm{RMSE} = \sqrt{\frac{\sum_{i=1}^{N}(\gamma_i-\beta_i)^2}{n}}$ |
| Relative Percent Deviation | RPD = SD/SEP |

Note: $x_i$ and $y_i$ are measured and predicted values, respectively; $\bar{x}$ and $\bar{y}$ represented the means measured and predicted values, respectively; and n is the number of samples.

## 3. Results and Analysis

### *3.1. Statistical Characteristics of the Sampling Data*

Soil electrical conductivity data (EC) were obtained using an EM38-MK2 m, and field measurements were taken at 353 points along 12 transects through the study area (showed in Figure 1). Based on an analysis of the original data, abnormal values that were caused by natural factors were eliminated to reduce their influence on the accuracy of the model. Subsequently, the data were divided into two subsets by uniform space. One subset was used for training ($n$ = 247), and the other subset was used for testing purposes ($n$ = 106). As can be seen in Figure 3, the mean values of EC that correspond to the calibration set and the validation set were 4.63 dS·m$^{-1}$ and 4.54 dS·m$^{-1}$, and the standard deviation (SD) was 1.99 dS·m$^{-1}$ and 2.20 dS·m$^{-1}$, respectively. The mean value from all field sampling points was 4.60 dS·m$^{-1}$, which is between the mean value both of calibration and validation sets.

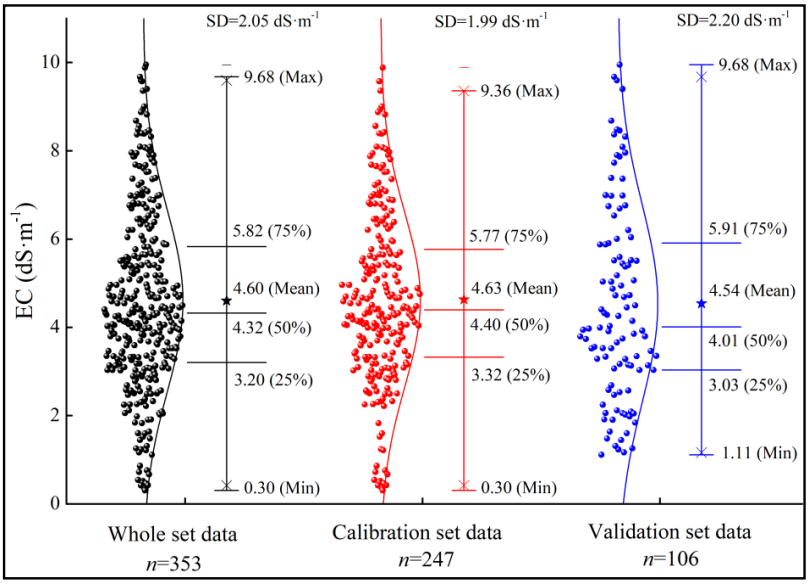


**Figure 3.** Statistical characteristics of the electrical conductivity (EC) of sampling points.

### *3.2. Analysis Correlation between EC and Bands of Worldview2-Images*

Based on the data source of the reflectance from remote sensing images and the measured soil electrical conductivity, five mathematical transformation methods were adopted to the remote sensing data, such as First Derivative (R-FD), Second Derivative (R-SD), Square data (R-SQ), Reciprocal inverse (1/R), and Reciprocal First Derivative (1/R-FD). The correlation between different transformation methods was analyzed. The relationship between EC and remote sensing data with its mathematical transformation was analyzed, as shown in Figure 4.

The reflectance of bands ((coastal) Band1, (blue) Band2, (green) Band3, (yellow) Band4, (red) Band5, (red edge) Band6, (near-IR1) Band7, and (near-IR2) Band8) corresponding to each sampling point were extracted by using the ENVI (Version 5.3) software, and correlation analysis was performed based on R-Programming. Figure 4a–c were the correlation results based on original data, R-FD data, and R-SD data, respectively. Among them, the R-FD data (Band5, Band6, Band7, and Band8) had a significant correlation with the EC data and the highest correlation was −0.51** ($p < 0.01$) whereas the R-SD data had a low correlation with the EC data and the highest correlation was −0.40** ($p < 0.01$). Figure 4d–f were the correlation results based on 1/R data, R-SQ data, and 1/R-FD data, respectively. Among them, the 1/R data and R-SQ data (Band6, Band7, and Band8) had a significant correlation with the EC data and the highest correlation was ±0.48** ($p < 0.01$) whereas the 1/R-FD data had a low correlation with the EC data and the highest correlation was 0.36** ($p < 0.01$). In the original data and 5 mathematical transformations, the highest correlation was selected as the sensitive bands and PLSR modeling variables.

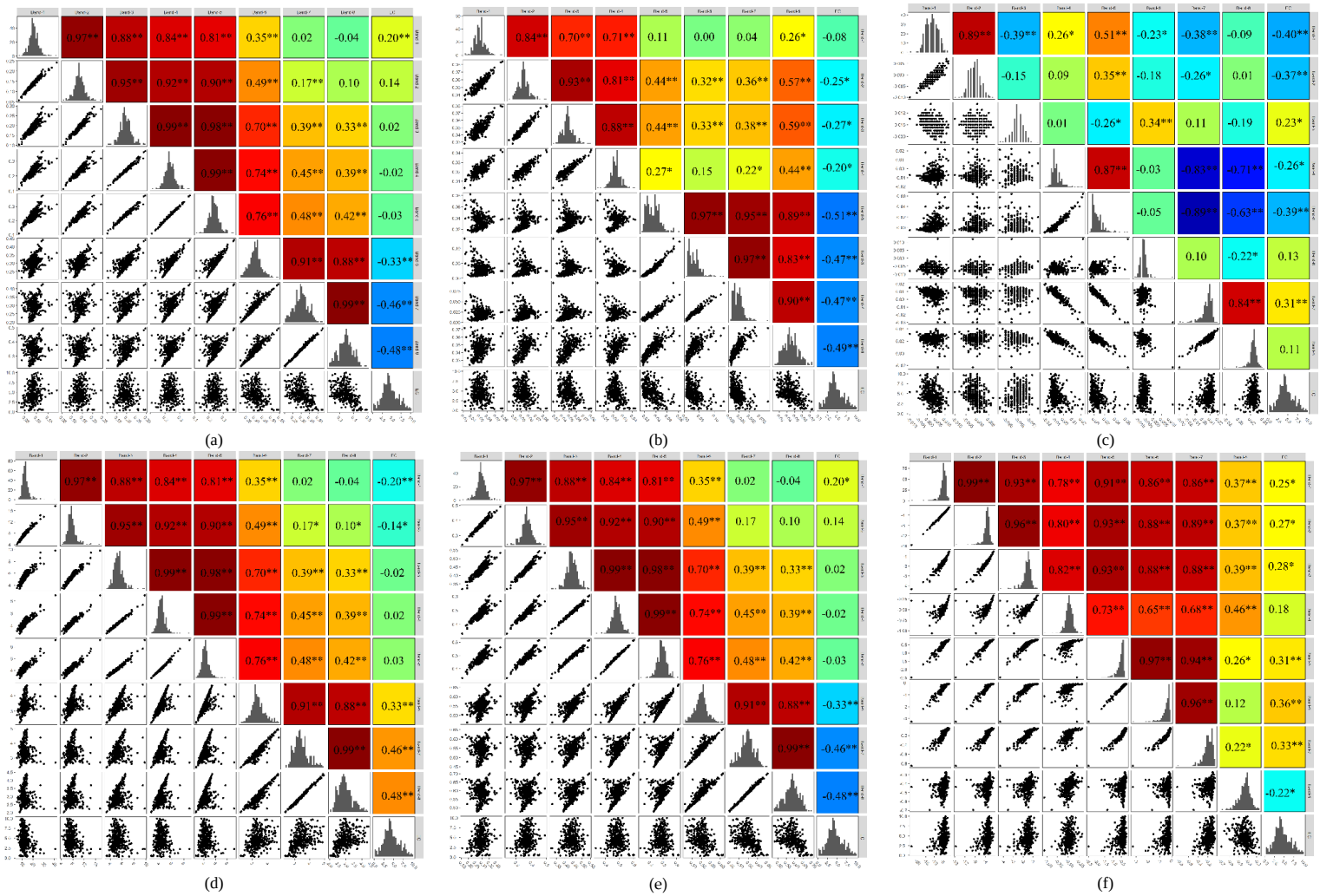


**Figure 4.** Correlation between EC and bands selected from Worldview-2 image: (**a**–**c**) the correlation results based on original data, first derivative (R-FD) data, and second derivative (R-SD) data, respectively, and (**d**–**f**) the correlation results based on reciprocal inverse (1/R) data, square data (R-SQ) data, and reciprocal first derivative (1/R-FD) data, respectively. Note: * a means pass the significant test (0.05), ** a means pass the significant test (0.01).

### *3.3. Analysis Correlation between EC and Optimized Spectral Index*

#### 3.3.1. Two-Dimensional Correlation Analysis

The optimized spectral indices (NDI, RI, and $SI_1$) selected in the study site were calculated from remote sensing data and an index that calculates all possible combinations as a pair of bands. Figures 5–10 summarized the correlation between optimized spectral indices and EC based on different mathematical methods. The X and Y axes represent $R_{\lambda 1}$ and $R_{\lambda 2}$, respectively, within the spectral region of 400–1040 nm. The color bar on the right indicates the mapping of the correlation coefficient values to the colormap. The upper and lower limits of the color bar are the maximum positive correlation coefficient and the maximum negative correlation coefficient, respectively.

In Figure 5, the optimized spectral indices based on R-data illustrated that the NDI and RI indices of band (B2, B3, B6, and B7) combinations had a good correlation with EC. The SI1 index of band (B7 and B8) combinations had a significant negative correlation with EC. The correlation coefficient ($p$ = 0.01) of optimum band combination indies ($NDI_{(B6,B2)}$, $RI_{(B6,B3)}$, and $SI_{1(B8,B8)}$) reached −0.45**, 0.45**, and 0.50**, respectively. In Figure 6, the optimized spectral indices based on R-FD data indicated a better correlation with EC. The correlation coefficient ($p$ = 0.01) of optimum band combination indies ($NDI_{(B7,B1)}$, $RI_{(B8,B7)}$, and $SI_{1(B5,B3)}$) reached −0.43**, −0.41**, and −0.54**, respectively.

As is shown in Figure 7, based on R-SD data, the optimal spectral combinations for NDI, RI, and SI1 indies provided a low correlation with EC data and the highest correlation coefficient reached ±0.3. In Figure 8, based on R-SQ data, the correlation coefficient ($p$ = 0.01) of optimal band combination indies ($NDI_{(B6,B2)}$, $RI_{(B6,B2)}$, and $SI_{1(B8,B7)}$) reached −0.45**, 0.45**, and −0.48**, respectively. In Figure 9, the optimized spectral indices based on 1/R data illustrated that the NDI and RI indice of band (B2, B3, B6, B7, and B8) combinations had a significant correlation with EC. The correlation coefficient ($p$ = 0.01) of optimal band combination indices ($NDI_{(B7,B2)}$, $RI_{(B5,B2)}$, and $SI_{1(B8,B8)}$) reached 0.45**, −0.46**, and 0.41**, respectively. The 1/R-FD data (Figure 10) illustrated that the optimized spectral indices (NDI and RI) provided the better correlation with EC than $SI_1$ index and that the maximum of correlation coefficient reached 0.41** ($NDI_{(B8,B5)}$), 0.42** ($RI_{(B8,B3)}$), and −0.34** ($SI_{1\ (B6,B4)}$).

Overall, the 2D correlation coefficients can provide additional detailed spectral information linked to EC. This band combination method further indicates that the optimal spectral combinations for NDI, RI, and $SI_1$ were relatively scattered and not concerned, but the correlation was significantly improved. The bands of Worldview-2 image identified as important features in the VIS-NIR region corresponded to B2, B3, B6, B7, and B8. These bands' combination is relatively related to the conductive elements in the soil.

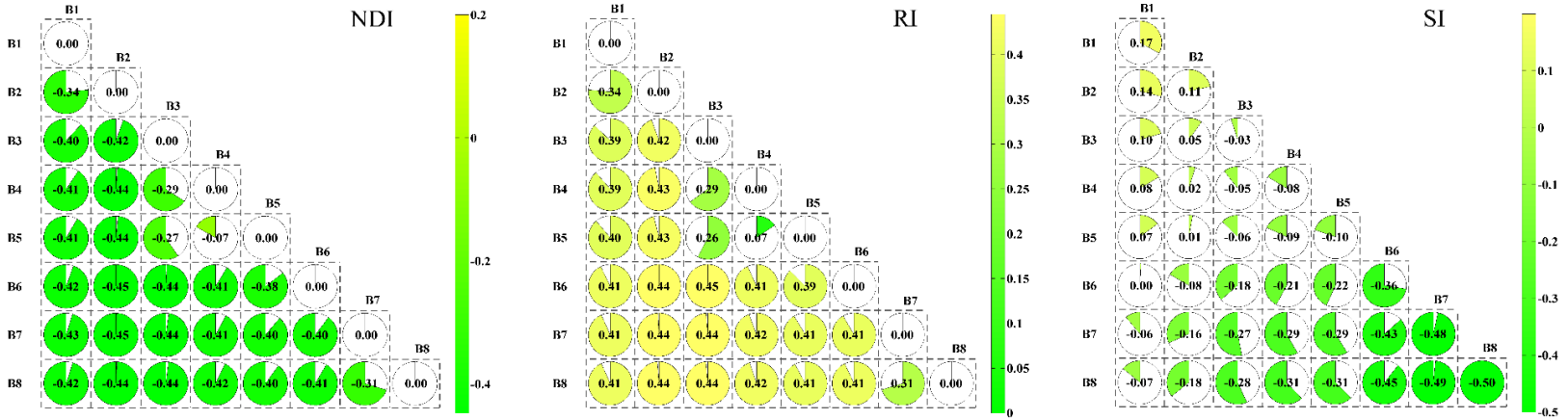


**Figure 5.** The correlation analysis between EC and optimized spectral indices based on original data (R). (**a**–**c**) represent the correlation EC with NDI, RI, and SI, respectively.

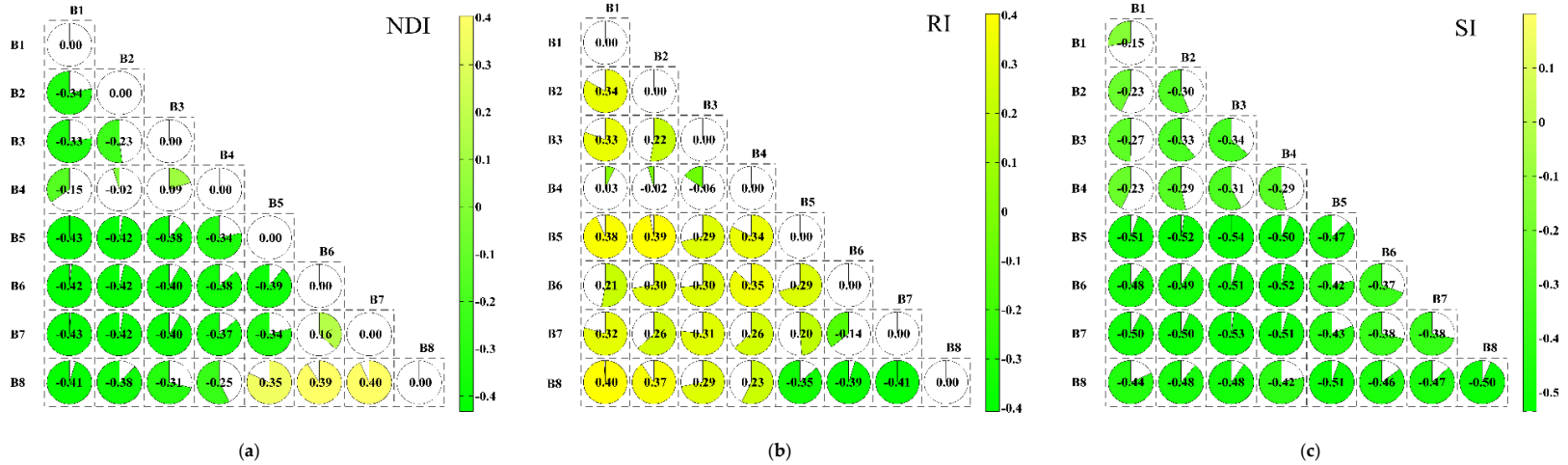


**Figure 6.** The correlation analysis between EC and optimized spectral indices based on first derivative (R-FD). (**a**–**c**) represent the correlation EC with NDI, RI, and SI, respectively.

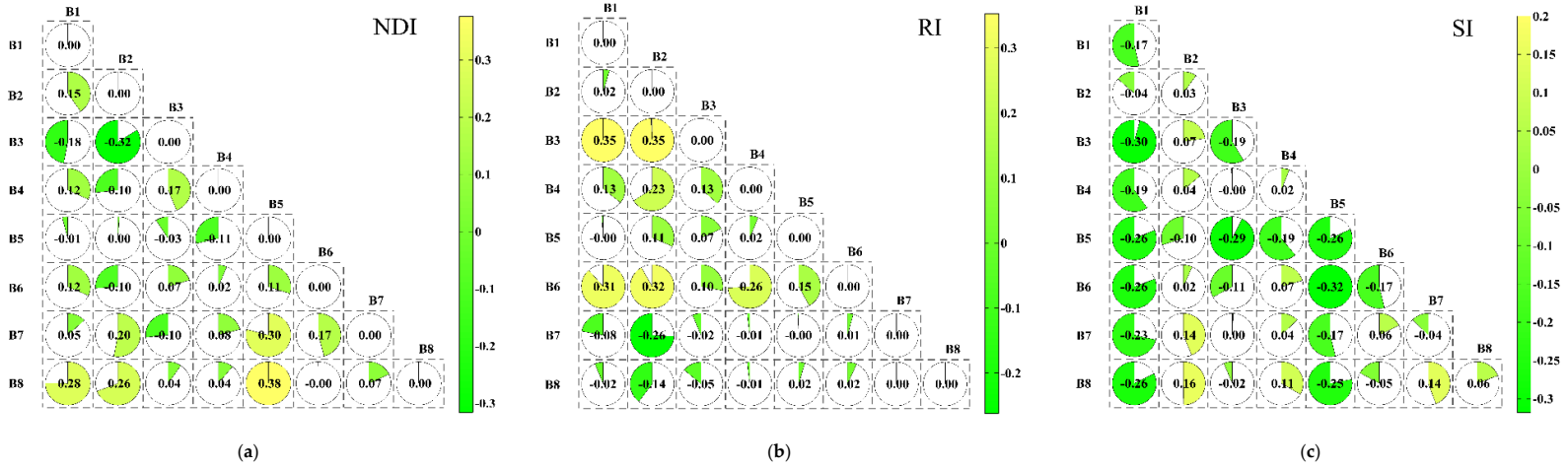


**Figure 7.** The correlation analysis between EC and optimized spectral indices based on second derivative (R-SD). (**a**–**c**) represent the correlation EC with NDI, RI, and SI, respectively.

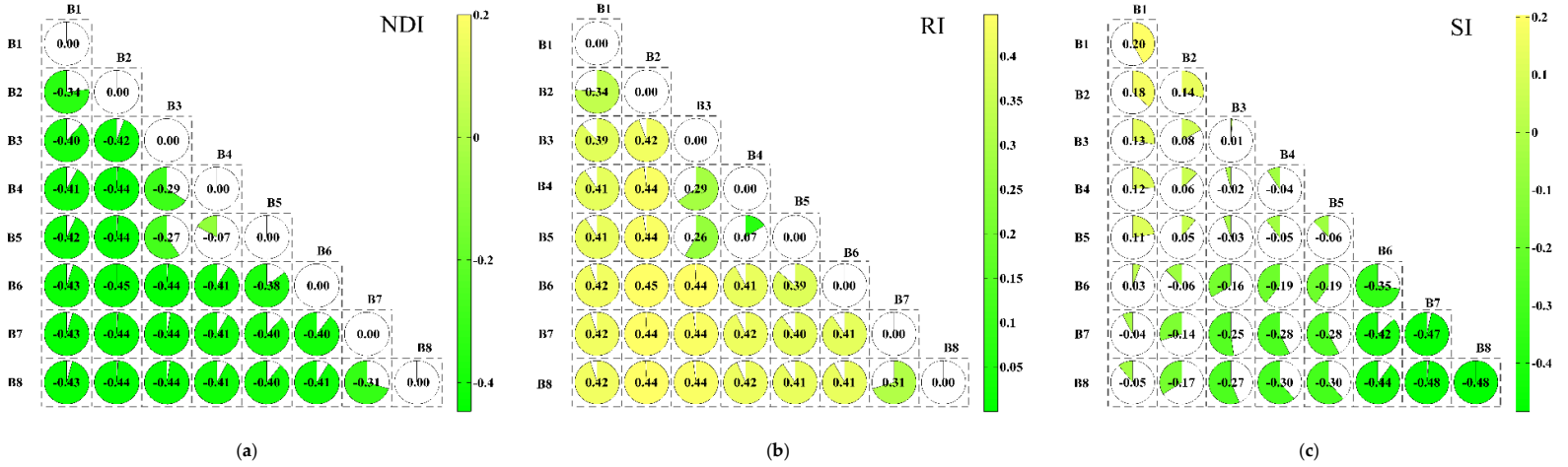


**Figure 8.** The correlation analysis between EC and optimized spectral indices based on square data (R-SQ). (**a**–**c**) represent the correlation EC with NDI, RI, and SI, respectively.

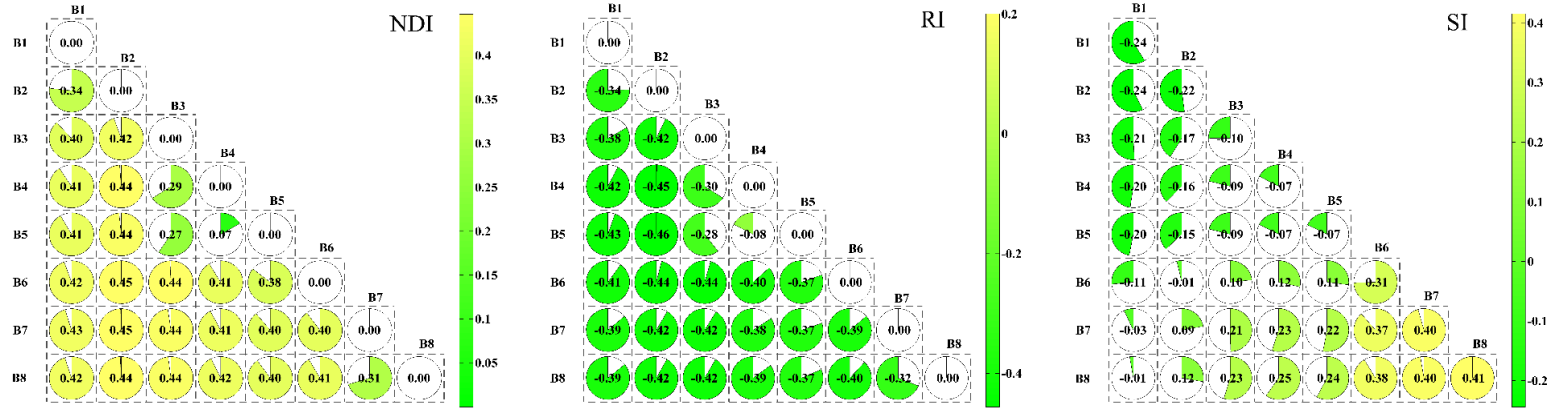


**Figure 9.** The correlation analysis between EC and optimized spectral indices based on reciprocal inverse (1/R). (**a**–**c**) represent the correlation EC with NDI, RI, and SI, respectively.

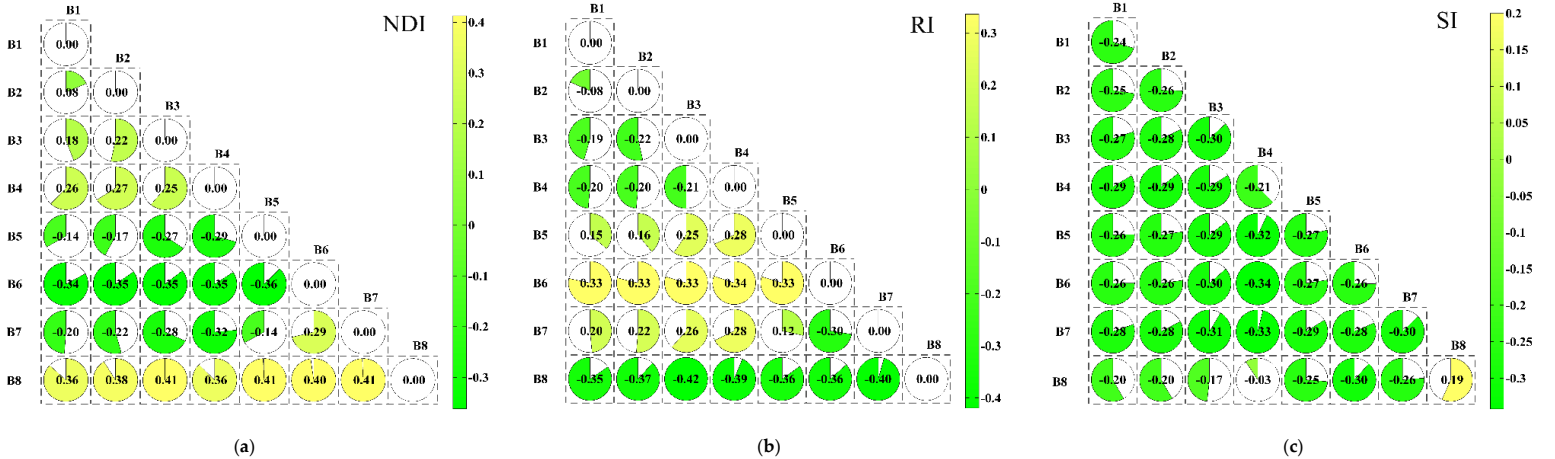


**Figure 10.** The correlation analysis between EC and optimized spectral indices based on reciprocal first derivative (1/R-FD). (**a**–**c**) represent the correlation EC with NDI, RI, and SI, respectively.

### 3.3.2. Three-Dimensional Correlation Analysis

The spectral indices ($SI_2$) selected in the study site were calculated from remote sensing data (spectral bands B1–B8) and an index that calculates based on the three-band combination in all possible combinations. The three-dimensional (3D) maps (showed in Figure 11) contained the horizontal slice map and vertical slice map, and the slice maps indicated the correlation between the EC and the spectral index ($SI_2$).

Optimal slice maps based on different mathematical methods (R-FD, R-SD, R-SQ, 1/R, and 1/R-FD) are shown in Figure 12a–f. The three axes in the slice maps delegate the reflectance of bands ($R_{\lambda 1}$ $R_{\lambda 2}$, and $R_{\lambda 3}$), respectively, within the spectral region of 400–1040 nm. The color bar on the right indicates the mapping of the correlation coefficient values to the colormap. The upper and lower limits of the color bar are the maximum positive correlation coefficient and the maximum negative correlation coefficient, respectively.

According to the correlation with EC, the optimal band combinations for $SI_2$ based on different mathematical methods were picked out. As can be seen from the slice maps, the combinations of the three-band usually inferred the better correlation. Thereinto, the most effective spectral indices ($SI_{2(B8,B8,B8)}$, $SI_{2(B5,B4,B4)}$, $SI_{2(B1,B5,B1)}$, $SI_{2(B8,B8,B8)}$, $SI_{2(B8,B8,B8)}$, and $SI_{2(B7,B7,B6)}$) based on different mathematical methods (R-FD, R-SD, R-SQ, 1/R, and 1/R-FD) had the significant correlation with maximum correlation coefficients of −0.48, −0.54, −0.35, −0.47, 0.44, and −0.34, respectively. Among all three-band indices, the Sqrt ($(B5)^2$ + $(B4)^2$ + $(B4)^2$) based on R-FD data has the best correlation coefficient with −0.54. Comparing to 2D indies, the three-band combination index enriched the data set and expanded the range of EC-related data.

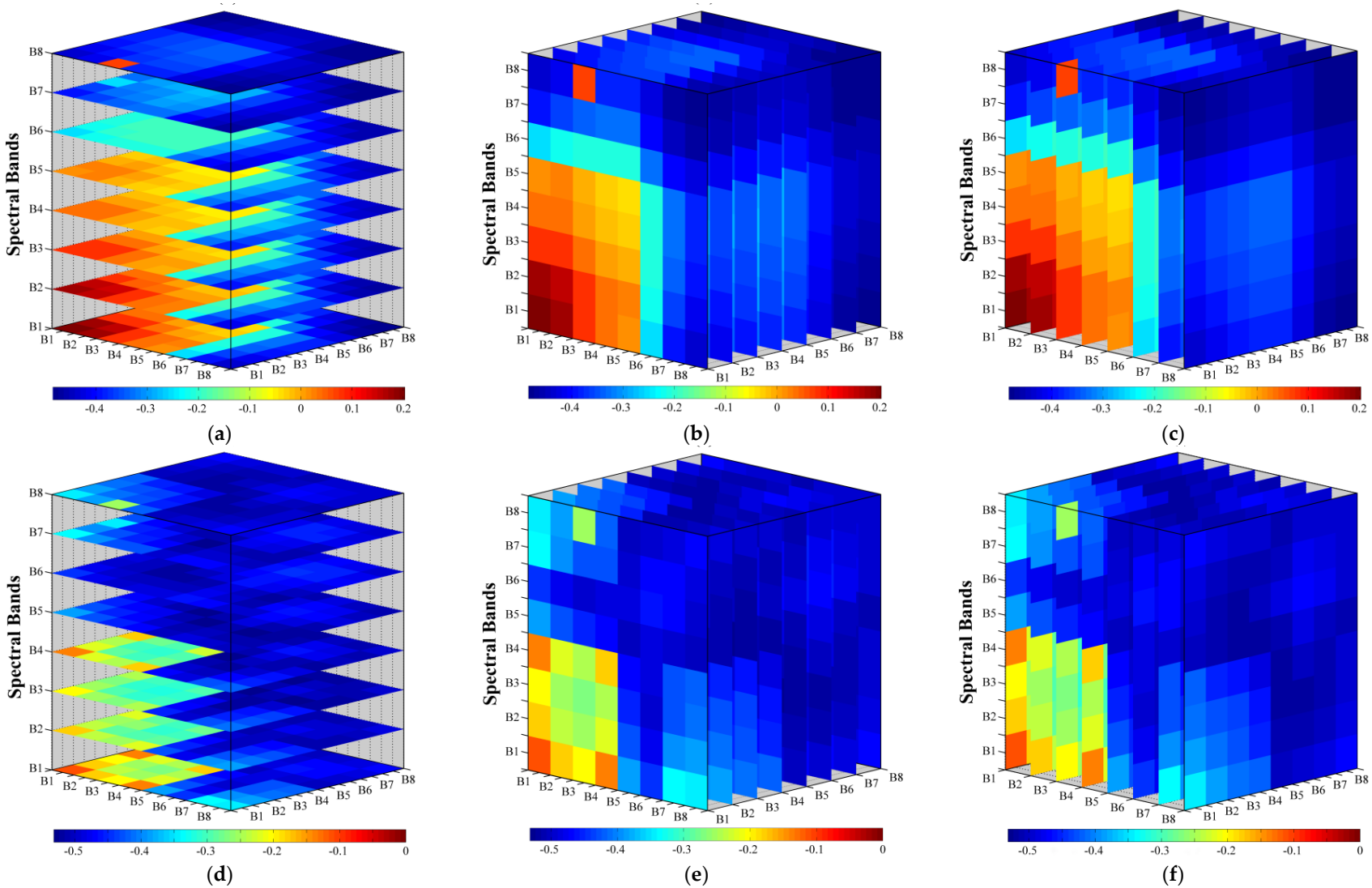


**Figure 11.** *Cont.*

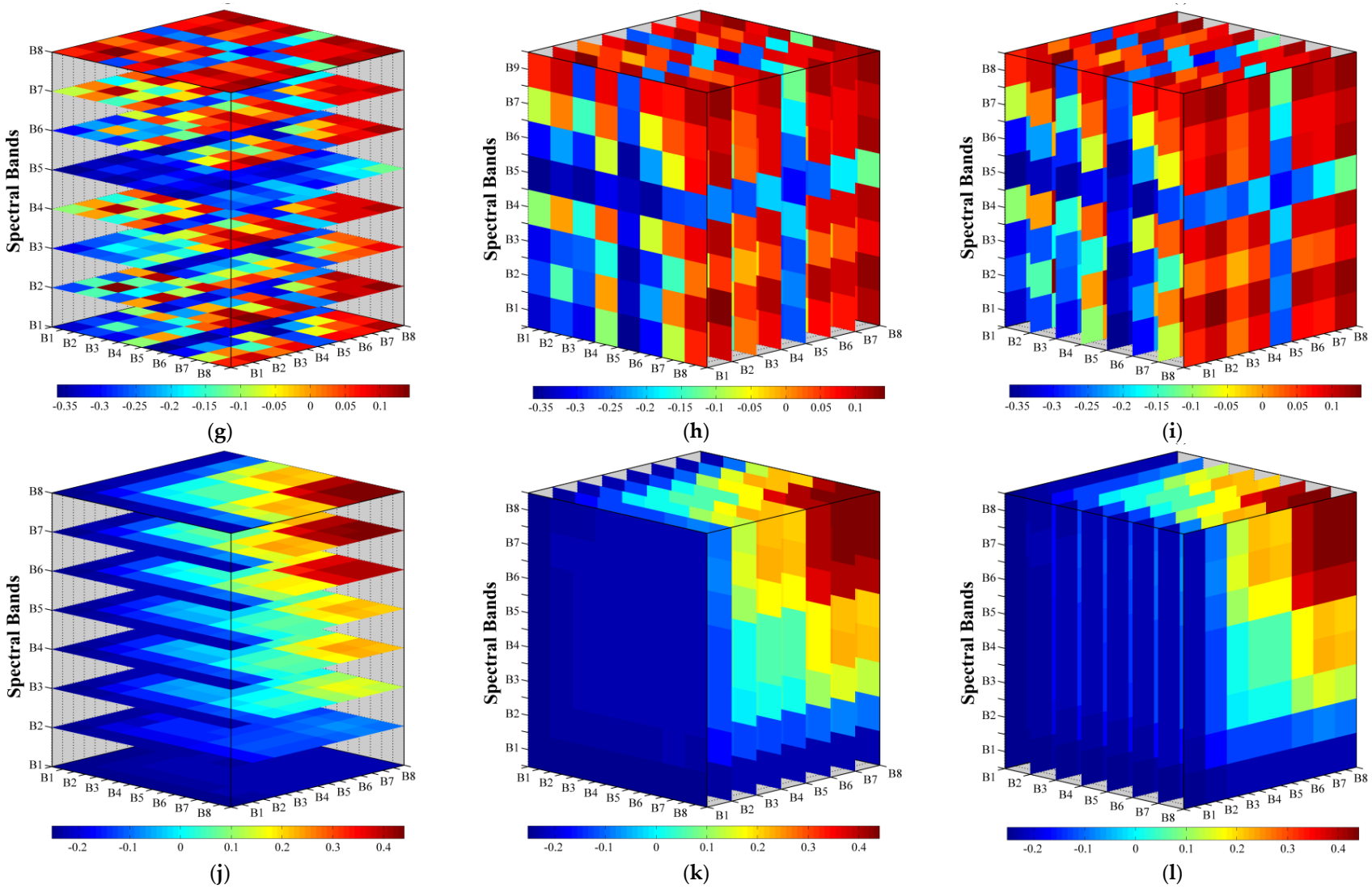


**Figure 11.** *Cont.*

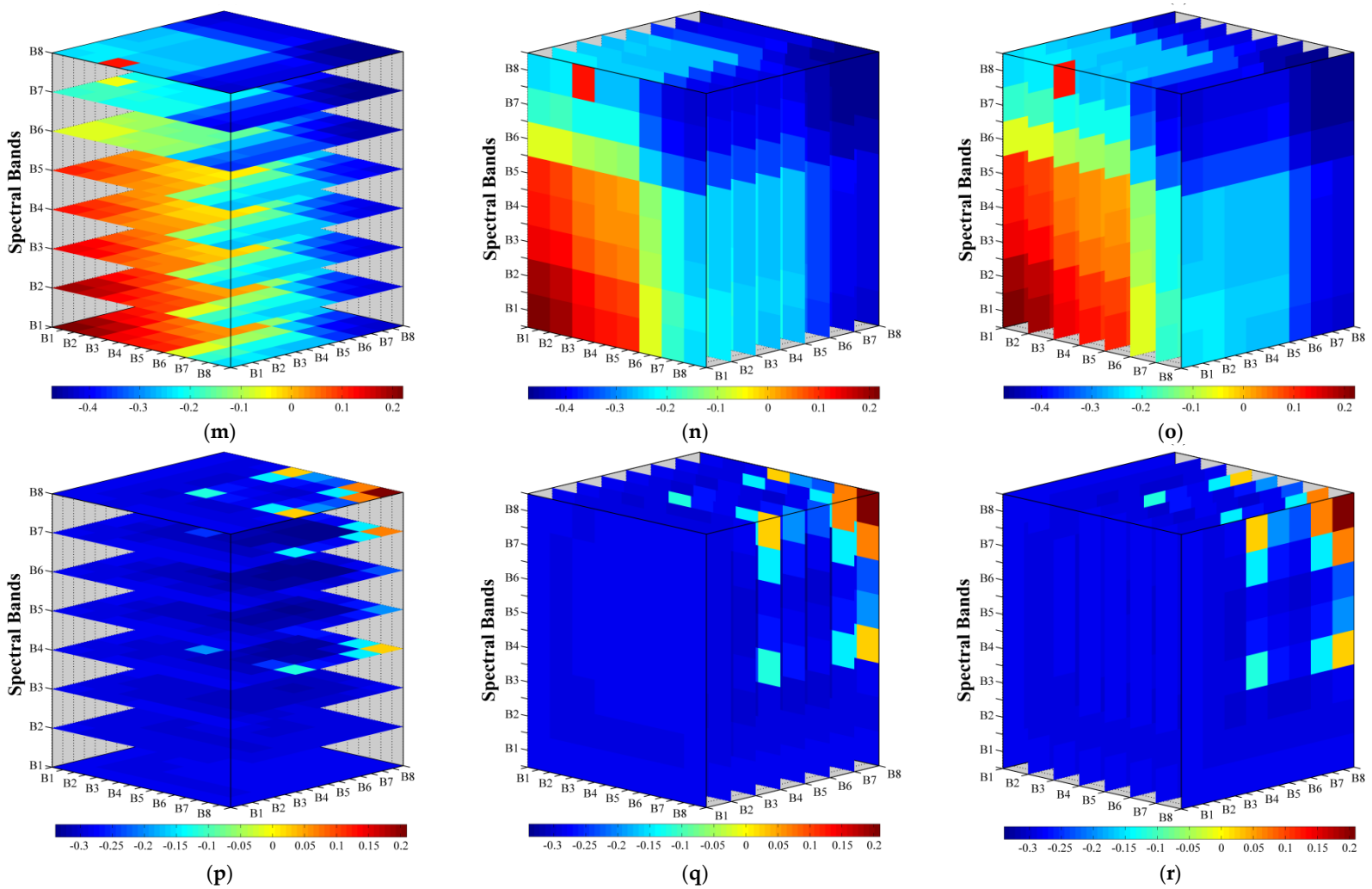


**Figure 11.** The correlation analysis between EC and optimized spectral indices based on different mathematical algorithms. (**a**–**r**) represent the horizontal slice map and vertical slice map, and the slice maps indicated the correlation between the EC and the spectral index ($SI_2$), respectively.

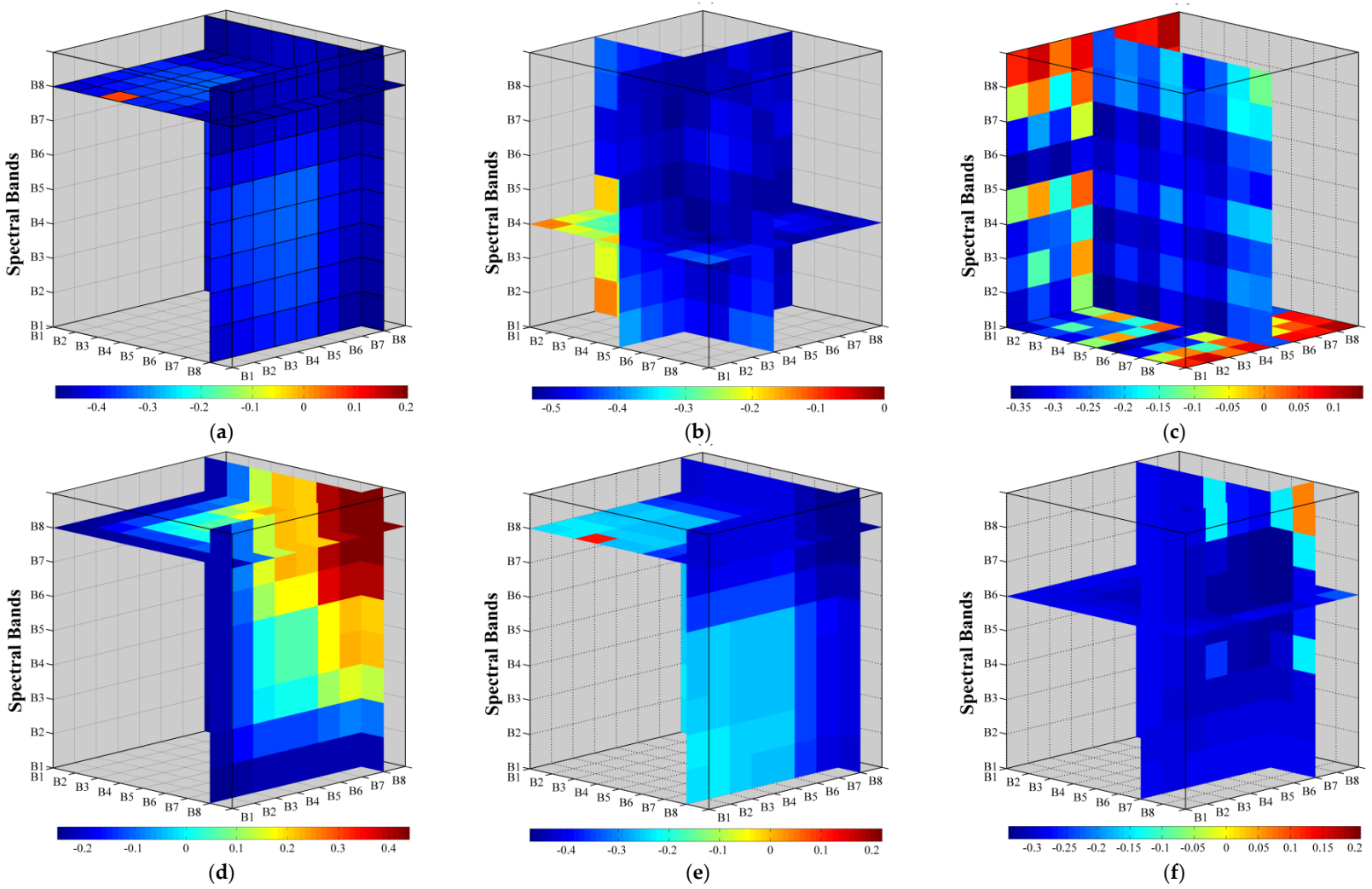


**Figure 12.** The correlation analysis between EC and optimized spectral indices based on reciprocal first derivative. (**a**–**f**) represent the correlation EC with SI2, respectively.

### *3.4. Estimation PLSR Models and Evaluation*

In the study site, we have one-dimensional (OD), two-dimensional (2D), and three-dimensional (3D) relations to analyze the correlation between EC and remote sensing data. In this process, the five mathematical algorithms used transmit remote sensing data: the spectral covariates (eight spectral bands, optimized spectral indices, optimized satellite soil salinity indices ($SI_1$), and optimized Three-Band Indices ($SI_2$)). We applied all the best correlation coefficients in each form of the transformation algorithms to build estimation models for salt-affected land estimation. The evaluation of the estimation models is illustrated (shown in Figure 13).

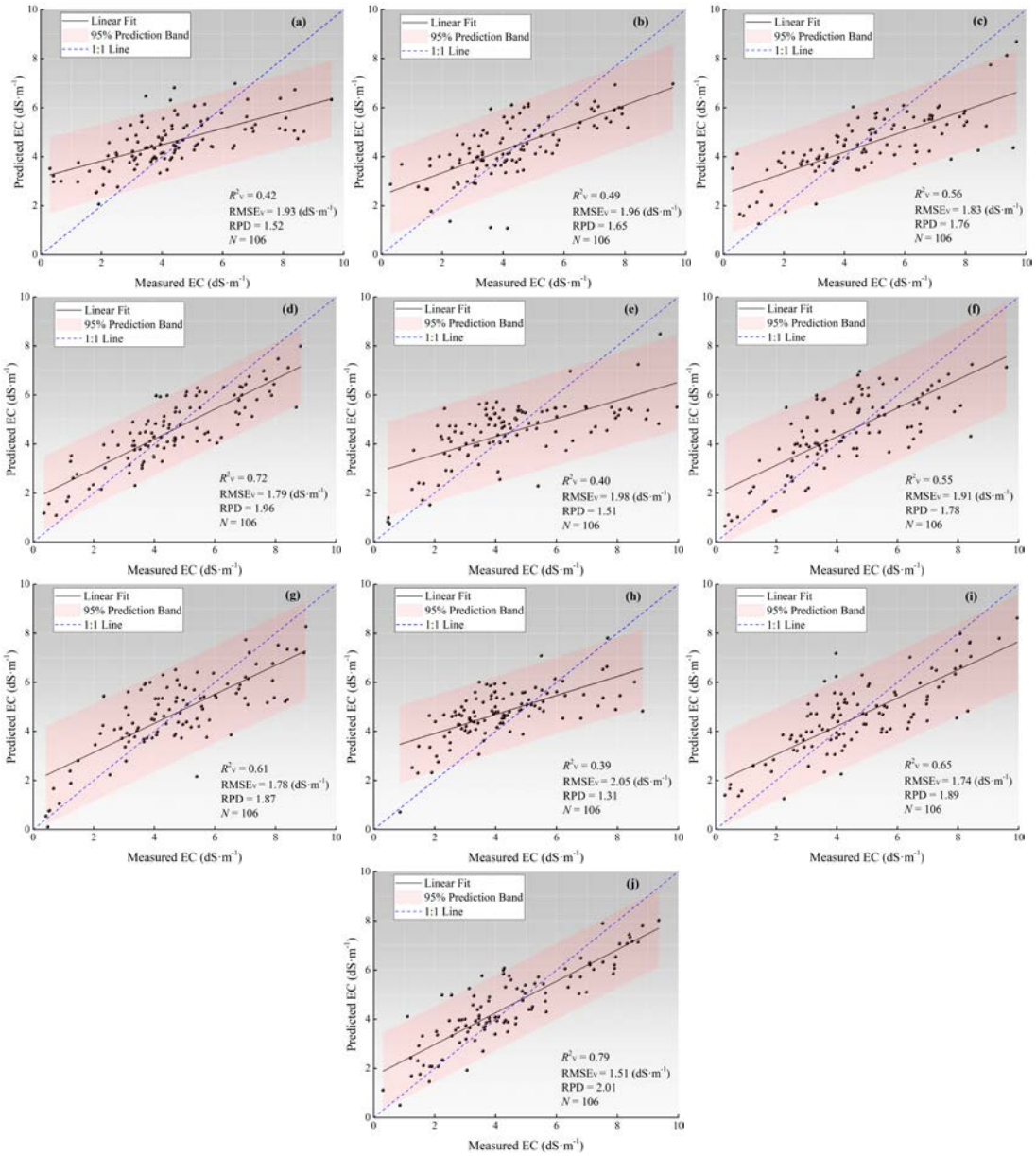


**Figure 13.** The scatter plot of measured versus predicted EC. (**a**) the result of Raw-I-PLSR model, (**b**) the result of Raw-II-PLSR model, (**c**–**h**) the results of (I-VI) PLSR models, (**i**) the result of α-PLSR model, and (**j**) the result of β-PLSR model.

The estimating performances of Raw-I-PLSR and Raw-II-PLSR models with 6 spectral parameters ($Band8_R$, $Band5_{R\text{-}FD}$, $Band1_{R\text{-}SD}$, $Band8_{R\text{-}SQ}$, $Band8_{1/R}$, and $Band6_{1/R\text{-}FD}$) indicates the low RPD values

of 1.52 and 1.65. The PLSR models (I-PLSR, II-PLSR, III-PLSR, IV-PLSR, V-PLSR, and VI-PLSR) and SI2-PLSR model were established in 2-dimensional and 3-dimensional data (2D and 3D), and the contrast of estimation models, indicating that predictive ability and stability of models in 2D and 3D, has been made better than in the Raw-PLSR model (shown in Table 4). The predictive ability of the $\beta$-PLSR performed the best result. The $\beta$-PLSR model has the highest $R^2_V$ value with 0.79 and the lowest $RMSE_V$ value with 1.51 dS·m$^{-1}$ and RPD value with 2.01. With the classification rule of RPD, it is the most effective model in this study site and the best-implemented model that met all the model selection and validation criteria and that was used to predict and map the spatial variation in soil salinity.

**Table 4.** The contrast of estimation models with soil salinity (ds·m$^{-1}$).

| Type | Acronym | Parameters | $R^2_c$ | $RMSE_c$ | $R^2_v$ | $RMSE_v$ | RPD |
|---|---|---|---|---|---|---|---|
| OD | Raw-I-PLSR | 4 | 0.45 | 1.81 | 0.42 | 1.93 | 1.52 |
| | Raw-II-PLSR | 3 | 0.49 | 1.84 | 0.49 | 1.96 | 1.65 |
| 2D | I-PLSR | 3 | 0.58 | 1.74 | 0.56 | 1.83 | 1.76 |
| | II-PLSR | | 0.76 | 1.76 | 0.72 | 1.79 | 1.96 |
| | III-PLSR | | 0.42 | 1.82 | 0.40 | 1.98 | 1.51 |
| | IV-PLSR | | 0.58 | 1.82 | 0.55 | 1.91 | 1.78 |
| | V-PLSR | | 0.63 | 1.75 | 0.61 | 1.78 | 1.87 |
| | VI-PLSR | | 0.43 | 1.97 | 0.39 | 2.05 | 1.31 |
| 3D | $\alpha$-PLSR | 4 | 0.69 | 1.73 | 0.65 | 1.74 | 1.89 |
| | $\beta$-PLSR | 3 | 0.80 | 1.40 | 0.79 | 1.51 | 2.01 |

Note: I, II, III, IV, V, and VI indicate that the spectral indices (NDI, RI, and $SI_1$) are optimized based on raw data and its mathematical transformation algorism (R-FD, R-SD, 1/R, R-SQ, and 1/R-FD). C represents calculation, V represents validation, and PLSR represents Partial least squares regression.

### *3.5. Soil Salinity Maps with EC Data*

The PLSR models calibrated in this study site were applied to map soil salinity with EC data and used the optimal PLSR model ($\beta$-PLSR) to build the spatial distribution of soil salinity in the study region (Figure 13). Furthermore, in accordance with the classification rules of soil electrical conductivity [31,32], the spatial classification map was further categorized into four levels of EC/dS·m$^{-1}$ (non-saline soil (0–2), slightly saline soil (2–4), moderately saline soil (4–8), and strongly saline soil (>8)). The salt-affected soil that is characterized by low or no-vegetation coverage demonstrated high EC values, and the higher the vegetation coverage, the lower the EC value (Figure 14). On the whole, the strongly EC value primarily occurs on both sides of the Keriya River. It also appears that the vegetation coverage played an imperative role in preventing soil salinization.

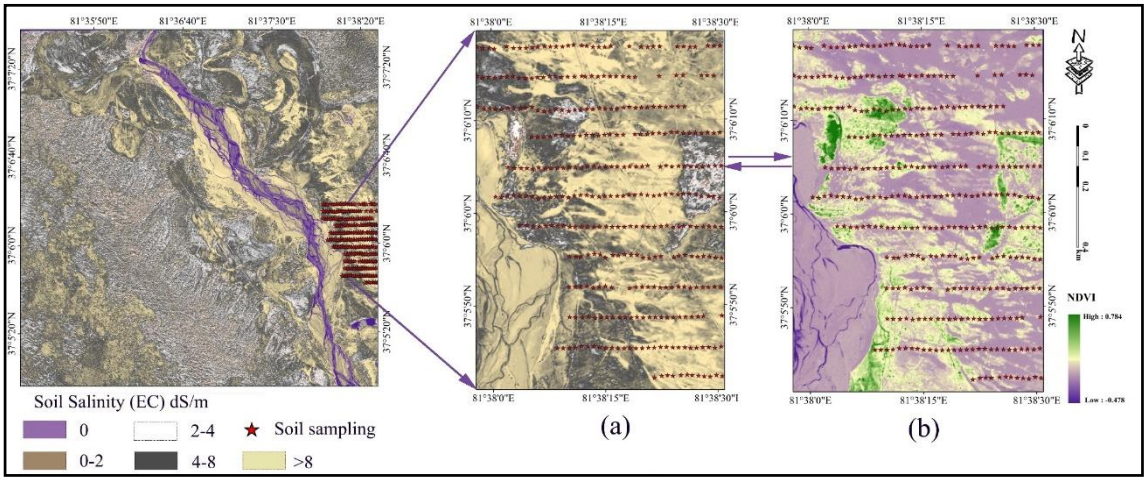


**Figure 14.** The soil salinity maps with EC data: (**a**) sampling area and EC inversion based on the optimal PLSR model and (**b**) sampling area based on Normalized Difference Vegetation Index (NDVI) inversion.

## 4. Discussion

### *4.1. Application of Multidimensional Modeling with Different Algorithm*

In recent studies, previously published spectral indices about salt-affected land have been used for monitoring soil salinization based on different images data, and remote sensing data includes VIS-NIR wavelengths in general [33]. The studies of soil salinization were carried out using different methods in arid and semiarid regions. For instance, Ding [34] established models based on Landsat images and EC data using universal kriging (UK) and a spectral index regression (SIR) ($R^2$ = 0.43, $R^2$ = 0.39). Combined with indices (SI, OLI-SI, and NDVI) and images (Landsat TM and ASTER), and Allbed A [13] indicated the possibility of applying IKONOS image and spectral indices (SAVI, NDSI, and SI-T) in the prediction of soil salinization using a stepwise regression method, and the results yielded $R^2$ = 0.65 and RMSE = 3.9 dS·m$^{-1}$.

Despite the hyperspectral remote sensing image and the consecutive spectral wide bands, it can only provide single salinization information and fixed spectral indices. Besides, the published spectral indices are not more sensitive to salt-affected land in different environmental conditions. The multi-spectral remote sensing images can provide effective data resources and advisable temporal resolution. Thereinto, the WV-2 image has high resolution and eight spectral wavebands. It is necessary to fully use high resolutions and its limited wavebands information; the OSI is the appropriate methods in mining of limited remote sensing data. For waveband information analysis of this study, the OSI is combined with different band information based on the fixed calculation formula. Increasing the relevance of OSI furthermore to the ground physical parameters such as EC is the main target. However, combined with high spatial resolution, image data and optimal spectral indices constructed the estimation PLSR model and performed the best results with $R^2_V$ = 0.79, RMSE$_V$ = 1.51 dS·m$^{-1}$, and RPD = 2.01, which could monitor and map the salt-affected land successfully in Keriya River regions.

### *4.2. Estimation of Salt-Affected Land in Arid and Semiarid Regions*

Salt-affected land is an appreciable effect by various environmental considerations, and severe salt-affected land eventually results in land desertification and lead to sustainable development of local agriculture [35]. In the study site, we analyzed the sensitivity of spectral wavebands from the WV-2 image to EC data and used all possible combined bands (2D and 3D indices) for estimating EC in the Keriya River areas. The results of Bannari [8] illustrated that the red band yields the best ability on features of salt-affected land. Our studies also showed that the red band based on R-FD data has a high relevance to EC; that the combined bands of 2D and 3D indices are mainly concentrated at red edge, near-IR1, near-IR2 in this study site; and that the results of study are similar to peer researchers' conclusion [13,36,37]. Eventually, it found that the two-band indices and three-band indices showed better results than other single spectral bands in this study.

More importantly, at the same time, the salinization information is quickly obtained through remote sensing data and soil salinization biological improvement measures are implemented promptly. The model generated high-resolution (2 m × 2 m) EC spatial distribution maps and revealed more details with salt-affected land than low spatial resolution. This study is expected to provide a method for the dynamic monitoring of soil salinization in arid or semiarid regions similar to the current study area. This method may need to adjust the spectral indicators according to local environmental conditions.

The remote sensing time series data is intended to be adopted in the future and to further improve the accuracy and stability of the estimation model for mapping salt-affected land in different stages. In addition to including different stages of data in a future study on this site, we also intend to focus on planning strategies for restoring the local ecological environment and for supporting sustainable development.

## 5. Conclusions

In this study, the predictive ability of WV-2 bands and OSI in the Keriya River Basin was investigated by using EC data collected in the field. The feature of spectral bands was extracted and tested, and the spectral band more sensitive to EC was determined to build different OSI (NDI and RI) and soil salinity indices ($SI_1$ and $SI_2$). Among these indices, the $SI_1$ (Sqrt($B3^2 \times B5^2$)) based on R-FD data has a higher correlation coefficient of −0.54. For the all three-band indices, the combinations of three bands usually revealed better correlation coefficients, and the $SI_2$ (Sqrt($B5^2 + B4^2 + B4^2$)) based on R-FD data has the best correlation coefficient of −0.54, indicating that leading into the red edge could enhance the sensitivity of the OSI to EC.

In arid and semiarid areas, OSI is an effective method to accurately monitor salt-affected land. Based on high spatial resolution (2 m × 2 m) of WV-2 and EC data, the PLSR models were constructed using different spectral indices, including reflectance of bands, published soil salinity index, and newly constructed OSI (2D index and 3D index).

The estimation ability changes with the input of different variable data, and the evaluation indexes of the RF-PLSR model are $R^2_V = 0.79$, $RMSE_V = 1.51$ dS·m$^{-1}$, and RPD = 2.01, which show the best state among the ten PLSR models. The field-tested results of soil salinity used to detect soil salinity based on optimal spectral index results in are good correlation with each other. Then, the finding of this study should help to control soil salinization and are further effective for soil restoration and land reclamation of this region and other similar arid regions.

**Author Contributions:** Funding acquisition, B.M.; Methodology, N.K.; Resources, A.A.; Software, N.K. and M.A.; Writing—review and editing, R.S. and C.D. All authors have read and agreed to the published version of the manuscript.

**Funding:** This study was supported by grants from the Youth Program of Natural Science Foundation of China (grant No.XJEDU2020Y037), College of Biology and Geography, Yili Normal University, YiNing, China and was supported by grants from the National Natural Science Foundation of China (grant No.41762019).

**Acknowledgments:** The authors would like to thank those who assisted long and strenuous hours to collect field data. The authors are also grateful to the reviewers for providing fruitful comments and suggestions.

**Conflicts of Interest:** The authors declare that there is no conflict of interests regarding the publication of this paper.

## References

1. Bot, A.J.; Nachtergaele, F.O.; Young, A. Land resource potential and constraints at regional and country levels. *World Soil Resour. Rep.* **2000**, *90*, 1–114. [CrossRef]
2. Wicke, B.; Sikkema, R.; Dornburg, V.; Faaij, A. Exploring land use changes and the role of palm oil production in Indonesia and Malaysia. *J. Land Use Policy* **2011**, *28*, 193–206. [CrossRef]
3. Abbas, A.; Khan, S.; Hussain, N.; Hanjra, M.A.; Akbar, S. Characterizing soil salinity in irrigated agriculture using a remote sensing approach. *J. Phys. Chem. Earth Parts A/B/C* **2013**, *55–57*, 43–52. [CrossRef]
4. Peng, J.; Biswas, A.; Jiang, Q.; Zhao, R.; Hu, J.; Hu, B.; Shi, Z. Estimating soil salinity from remote sensing and terrain data in southern Xinjiang Province, China. *J. Geoderma* **2019**, *337*, 1309–1319. [CrossRef]
5. Douaoui, A.E.K.; Nicolas, H.; Walter, C. Detecting salinity hazards within a semiarid context by means of combining soil and remote-sensing data. *J. Geoderma* **2006**, *134*, 217–230. [CrossRef]
6. Ma, L.; Yang, S.; Simayi, Z.; Gu, Q.; Li, J.; Yang, X.; Ding, J. Modeling variations in soil salinity in the oasis of Junggar Basin, China. *J. Land Degrad. Dev.* **2018**, *29*, 551–562. [CrossRef]
7. Aldabaa, A.A.A.; Weindorf, D.C.; Chakraborty, S.; Sharma, A.; Li, B. Combination of proximal and remote sensing methods for rapid soil salinity quantification. *J. Geoderma* **2015**, *239–240*, 34–46. [CrossRef]
8. Bannari, A.; El-Battay, A.; Bannari, R.; Rhinane, H. Sentinel-MSI VNIR and SWIR bands sensitivity analysis for soil salinity discrimination in an arid landscape. *J. Remote Sens.* **2018**, *10*, 855. [CrossRef]
9. Peng, J.; Xiang, H.; Guo, Y.; Shi, Z. Comparative study on hyperspectral inversion accuracy of soil salt content and electrical conductivity. *J. Spectrosc. Spectr. Anal.* **2014**, *34*, 510–514.
10. Ge, X.; Wang, J.; Ding, J.; Cao, X.; Zhang, Z.; Liu, J.; Li, X. Combining UAV-based hyperspectral imagery and machine learning algorithms for soil moisture content monitoring. *J. PeerJ* **2019**, *7*, e6926. [CrossRef]

11. Khan, N.M.; Rastoskuev, V.V.; Sato, Y.; Shiozawa, S. Assessment of hydrosaline land degradation by using a simple approach of remote sensing indicators. *J. Agric. Water Manag.* **2005**, *77*, 96–109. [CrossRef]
12. Kallel, A.; Ksibi, M.; Dhia, H.B.; Khélifi, N. Erratum to: Recent Advances in Environmental Science from the Euro-Mediterranean and Surrounding Regions. In *Euro-Mediterranean Conference for Environmental Integration*; Springer International Publishing: Cham, Switzerland, 2017.
13. Allbed, A.; Kumar, L.; Aldakheel, Y.Y. Assessing soil salinity using soil salinity and vegetation indices derived from IKONOS high-spatial resolution imageries: Applications in a date palm dominated region. *J. Geoderma* **2014**, *230–231*, 1–8. [CrossRef]
14. Triki Fourati, H.; Bouaziz, M.; Benzina, M.; Bouaziz, S. Modeling of soil salinity within a semi-arid region using spectral analysis. *Arab. J. Geosci.* **2015**, *8*, 11175–11182. [CrossRef]
15. Odeh, I.O.A.; Onus, A. Spatial analysis of soil salinity and soil structural stability in a semiarid region of new south wales, Australia. *J. Environ. Manag.* **2008**, *42*, 265–278. [CrossRef] [PubMed]
16. Ghulam, A.; Qin, Q.; Zhu, L.; Abdrahman, P. Satellite remote sensing of groundwater: Quantitative modelling and uncertainty reduction using 6s atmospheric simulations. *Int. J. Remote Sens.* **2004**, *25*, 5509–5524. [CrossRef]
17. Kasim, N.; Tiyip, T.; Abliz, A.; Nurmemet, I.; Sawut, R.; Maihemuti, B. Mapping and modeling of soil salinity using worldview-2 data and em38-km2 in an arid region of the keriya river, China. *J. Photogramm. Eng. Remote Sens.* **2018**, *12*, 43–52. [CrossRef]
18. Abdulla, A.; Abduwasit, G.; Ümüt, H.; Jian-li, D.; Mamat, S.; Fei, Z.; Ilyas, N.; Abdugheni, A. Effects of shallow groundwater table and salinity on soil salt dynamics in the Keriya Oasis, Northwestern China. *J. Environ. Earth Sci.* **2016**, *75*, 1–15.
19. Wang, F.; Yang, S.; Yang, W.; Yang, X.; Jianli, D. Comparison of machine learning algorithms for soil salinity predictions in three dryland oases located in xinjiang uyghur autonomous region (Xjuar) of China. *Eur. J. Remote Sens.* **2020**, *52*, 256–276. [CrossRef]
20. Corwin, D.L.; Lesch, S.M.; Oster, J.D.; Kaffka, S.R. Short-term sustainability of drainage water reuse: Spatio-temporal impacts on soil chemical properties. *J. Environ. Qual.* **2008**, *37*, S8–S24. [CrossRef]
21. Sidike, A.; Zhao, S.; Wen, Y. Estimating soil salinity in pingluo county of China using quickbird data and soil reflectance spectra. *Internat. J. Appl. Earth Obser. Geoinformat.* **2014**, *26*, 156–175. [CrossRef]
22. Guo, S.; Ruan, B.; Chen, H.; Guan, X.; Wang, S.; Xu, N. Characterizing the spatiotemporal evolution of soil salinization in hetao irrigation district (China) using a remote sensing approach. *Int. J. Remote Sens.* **2018**, *39*, 6805–6825. [CrossRef]
23. Inoue, Y.; Sakaiya, E.; Zhu, Y. Diagnostic mapping of canopy nitrogen content in rice based on hyperspectral measurements. *Remote Sens. Environ.* **2012**, *126*, 210–221. [CrossRef]
24. Haaland, D.M.; Thomas, E.V. Partial least-squares methods for spectral analyses: 2. Application to simulated and glass spectral data. *Anal. Chem.* **1988**, *60*, 1202–1208. [CrossRef]
25. Kahaer, Y.; Tashpolat, N. Estimating Salt Concentrations Based on Optimized Spectral Indices in Soils with Regional Heterogeneity. *J. Spectrosc.* **2019**, *2019*, 15. [CrossRef]
26. Maimaitiyiming, M.; Ghulam, A.; Bozzolo, A. Early detection of plant physiological responses to different levels of water stress using reflectance spectroscopy. *J. Remote Sens.* **2017**, *9*, 745. [CrossRef]
27. Li, S.; Shi, Z.; Chen, S.; Ji, W.; Zhou, L.; Yu, W. In situ measurements of organic carbon in soil profiles using vis-nir spectroscopy on the qinghai–tibet plateau. *Environ. Sci. Technol.* **2015**, *49*, 4980–4987. [CrossRef]
28. Karunaratne, S.B.; Bishop, T.F.A.; Baldock, J.A.; Odeh, I.O.A. Catchment scale mapping of measurable soil organic carbon fractions. *J. Geoderma* **2014**, *S219-220*, 14–23. [CrossRef]
29. Nawar, S.; Buddenbaum, H.; Hill, J. Digital mapping of soil properties using multivariate statistical analysis and aster data in an arid region. *J. Remote Sens.* **2015**, *7*, 1181–1205. [CrossRef]
30. Chang, C.-W.; Laird, D.A.; Mausbach, M.J.; Hurburgh, C.R. Near-infrared reflectance spectroscopy–principal components regression analyses of soil properties. *SSSA* **2000**, *65*, 480–490. [CrossRef]
31. Williams, B.; Walker, J.; Anderson, J. Spatial variability of regolith leaching and salinity in relation to whole farm planning. *Aust. J. Exp. Agric.* **2006**, *46*, 1271–1277. [CrossRef]
32. Farifteh, J.; Meer, F.V.D.; Atzberger, C.; Carranza, E.J.M. Quantitative analysis of salt-affected soil reflectance spectra: A comparison of two adaptive methods (PLSR and ANN). *J. Remote Sens. Environ.* **2007**, *110*, 59–78. [CrossRef]

33. Hong, Y.; Liu, Y.; Chen, Y.; Liu, Y.; Yu, L.; Liu, Y.; Cheng, H. Application of fractional-order derivative in the quantitative estimation of soil organic matter content through visible and near-infrared spectroscopy. *J. Geoderma* **2019**, *337*, 758–769. [CrossRef]
34. Ding, J.; Yu, D. Monitoring and evaluating spatial variability of soil salinity in dry and wet seasons in the Werigan–Kuqa Oasis, China, using remote sensing and electromagnetic induction instruments. *J. Geoderma* **2014**, *235–236*, 316–322. [CrossRef]
35. Gorji, T.; Tanik, A.; Sertel, E. Soil salinity prediction, monitoring and mapping using modern technologies. *J. Procedia Earth Planet. Sci.* **2015**, *15*, 507–512. [CrossRef]
36. Hu, J.; Peng, J.; Zhou, Y.; Xu, D.; Zhao, R.; Jiang, Q.; Fu, T.; Wang, F.; Shi, Z. Quantitative estimation of soil salinity using UAV-borne hyperspectral and satellite multispectral images. *J. Remote Sens.* **2019**, *11*, 736. [CrossRef]
37. Doolittle, J.A.; Brevik, E.C. The use of electromagnetic induction techniques in soils studies. *J. Geoderma* **2014**, *223–225*, 33–45. [CrossRef]